Charge and Compositional Effects on the 2D–3D Transition in Octameric AgAu Clusters

Heard, Christopher; Shayeghi, Armin; Schaefer, Rolf; Johnston, Roy

DOI:
10.1515/zpch-2015-0721

Document Version
Publisher's PDF, also known as Version of record

Citation for published version (Harvard):
Heard, C, Shayeghi, A, Schaefer, R & Johnston, R 2016, 'Charge and Compositional Effects on the 2D–3D Transition in Octameric AgAu Clusters', *Zeitschrift fur Physikalische Chemie*, vol. 230, no. 5-7, pp. 955–975. https://doi.org/10.1515/zpch-2015-0721

Christopher Heard*, Armin Shayeghi, Rolf Schäfer, and Roy Johnston

Charge and Compositional Effects on the 2D–3D Transition in Octameric AgAu Clusters

DOI 10.1515/zpch-2015-0721
Received October 23, 2015; accepted November 22, 2015

Abstract: The unbiased density functional-based Birmingham Cluster Genetic Algorithm is employed to locate the global minima of all neutral and mono-ionic silver-gold octamer clusters. Structural, energetic and electronic trends are determined across the series, in order to clarify the role of composition and charge on the position of the 2D–3D transition in ultrasmall coinage metal systems. Our calculations indicate a preference for three dimensional structures at high silver concentrations, which varies significantly with charge. The minimum in composition dependent mixing energies is independent of the charge, however, with a preference for the maximally mixed clusters, $Ag_4Au_4^{\nu}$ for all charge states ν. The sensitivity of isomeric preference to ν is found to be greater for electron-rich and electron-deficient clusters, implying a complexity of unambiguous determination of cluster motifs in related experiments. Vertical ionization potentials and detachment energies are calculated to probe electronic behaviour, providing numerical predictions for future spectroscopic studies.

Keywords: Genetic Algorithm, Global Optimisation, Bimetallic Clusters, Range-Separated DFT, Ionization Potentials.

Dedicated to Professor Michael Springborg on the occasion of his 60th birthday

***Corresponding author: Christopher Heard,** Department of Applied Physics, Chalmers University of Technology, Göteborg, SE-41296, Sweden, e-mail: christopher.heard@chalmers.se
Armin Shayeghi, Rolf Schäfer: Eduard-Zintl-Institut, Technische Universität Darmstadt, Alarich-Weiss-Straße 8, 64287 Darmstadt, Germany
Roy Johnston: School of Chemistry, University of Birmingham, Edgbaston, B15 2TT, United Kingdom

1 Introduction

In the field of cluster physics, coinage metal clusters are of fundamental interest, due to their particular electronic structure. With an open shell $d^{10}s^1$ electronic configuration, and a significant degree of s-d orbital hybridisation, the divide between simple s-metals and transition metals is blurred. Further, the tunability of this electronic feature by varying particle size, charge and shape, manifests itself in a wide variety of applications. Current examples for coinage metal particles include nanophotonics [1, 2], sensing [3], catalysis [4, 5], and biodiagnostics [6, 7]. From a fundamental perspective, they represent ideal model systems for studying ultrasmall metallic particles [2, 8, 9], owing to their relative stability and ease of experimental investigation.

Several experimental studies have been performed for small coinage metal clusters, from laser-induced fluorescence spectroscopy [10], to photoelectron spectroscopy [11–14], photodissociation [15–17] and infrared [18, 19] photon detachment spectroscopy. Structural properties have been studied in ion mobility experiments [20], and related theoretical analysis [21, 22], from which results can be interpreted by means of charge-transfer and entropic effects. From a chemical point of view, reactivities of mixed gold-silver clusters towards carbon monoxide oxidation have been studied [23], and the importance of silver atoms for the coadsorption of carbon monoxide and water in the water-gas shift reaction has also been described [24]. Optically, doping small silver clusters with gold has an enormous influence [25], while doping the Au_{20} cluster with silver atoms shifts the HOMO-LUMO gap towards lower energies [26]. For larger Ag_nAu_m ($m + n$ = 20, 37, 55, 147) clusters, a vanishing surface plasmon-like resonance of the pure silver species results in a yet more complex optical behaviour [27, 28].

The situation becomes generally more complicated in such nanoalloy clusters, in which composition and chemical ordering play an additional role. These materials may exhibit interesting optical and catalytic properties but locating the GM is made more difficult by the existence of a large number of different shapes and homotops for each composition. The position of the 2D to 3D structural transition as a function of composition for eight atom neutral gold-silver clusters has been studied [29]. A density functional global optimisation study of neutral 8-atom Cu-Ag and Cu-Au clusters has shown sharper and earlier appearing topological transitions in doping series when compared to gold-silver particles [30]. Experimentally, Wang et al. [12, 14] have probed the effect of isoelectronic doping of coinage metals into gold, finding a reduction in onset size for the transition. The recent global optimisation study of Munoz et al. [31] for neutral $Au_{13-n}Ag_n$ clusters has suggested that there is close energetic competition between isomers across

the composition range. Interestingly, the authors find that the overall trends in binding energy, transition point and electronic structure are quite insensitive to functional, isomer choice and the use of spin orbit coupling. Overall, however, the position of the 2D–3D transition in small coinage metal bimetallic clusters, and the sensitivity to charge state and composition remains unresolved.

In this study, the dimensionality transition of $Ag_nAu_m^{\nu}$ $(n + m = 8)$ clusters is studied as a function of their charge state $\nu = 0, \pm 1$, with range-separated DFT and global optimisation techniques, in order to understand the influence of charge and composition on structural properties. These cluster structures therefore represent the local minima potentially available to cluster beam measurements, in which clusters are produced and interrogated in vacuum. Vertical ionization and electronic detachment energies are calculated. The influence of composition, structure and the effect of homotops are discussed.

2 Computational details

The computational methodology employed in the global optimisation of cluster structure with the DFT variant of the Birmingham Cluster Genetic Algorithm (BCGA) has been described in previous articles [29, 32]. Key aspects of the method are as follows: The plane-wave self consistent field (PWscf) code within the Quantum Espresso (QE) package [33], has been coupled with the Lamarckian BCGA [34] to perform direct cluster global optimisation at the DFT level of theory. Ultrasoft Rabe–Rappe–Kaxiras–Joannopoulos pseudopotentials [35] are used to represent the core wavefunctions, which model the 36 and 68 core electrons for Ag and Au atoms, respectively, while 11 valence electrons are explicitly treated for each atom. An additional nonlinear correction is applied for gold and the Perdew–Burke–Ernzerhof (PBE) [36] xc functional is employed within the generalized gradient approximation (GGA) framework of spin-unrestricted DFT. Local optimization of cluster structures is performed, with an electronic self consistency criterion of 10^{-5} eV, and total energy and force convergence considered to be reached when below the threshold values of 10^{-3} eV and 10^{-2} eV/Å, respectively. A Methfessel–Paxton smearing scheme [37], expanded to first order, is utilised to aid electronic convergence. The BCGA is then run until the generational convergence criterion is met. This criterion is one of stagnation: that the lowest energy structure in a generation has not varied in the previous five consecutive full generations. Sorting of duplicate structures is found to play a significant role in maintaining genetic diversity for the small generations used in DFT-GA searches, and so a sorting scheme is used, in which duplicate structures in a generation are removed based both on

energetic similarity and the moments of inertia of the cluster. For periodic calculations, a fictitious, uniform Jellium background charge must be included in order to counteract the charge upon the cluster, and re-establish neutrality over the entire cell. This is a potential source of error for the calculations, and is minimised by imposing a large unit cell, in which the electrostatic potential is stabilised.

Several of the lowest lying structures, each of which are potential candidates for the GM, are subsequently locally optimized with the NWChem v6.1 code [38], employing an extensive 19-electron def2-TZVPP basis set and the corresponding effective core potential (def2-ECP) [39]. Open shell calculations were performed with the spin-unrestricted DFT formalism at low spins. Spin values were selected based on test calculations involving geometry reoptimisation at several spin states, in which higher values generally induced destabilisations of greater than 1 eV. Time-dependent DFT (TDDFT) calculations were made to determine HOMO-LUMO gaps for a sample of compositions. These gaps were in excess of 1 eV, providing additional evidence for the accuracy of the single reference method applied in this work. For local geometry optimisation, we employ the LC-ωPBEh xc functionals which have recently shown a great deal of promise for the calculation of structures and spectral properties of Au, Ag and AuAg clusters [16, 40–43]. LC-ωPBEh is a modified version of the range separated LC-ωPBE xc functional, which separates the exchange term into long range and short range contributions in order to recover the asymptotic $1/r$ behaviour at large distances of the electrons from the nucleus [40, 44]. Scalar relativistic corrections are included in our computational setup, both in the pseudopotentials of the initial GO search, and the effective core potentials of the later refinement calculations.

For charged species, which commonly exhibit a rich manifold of structures within a narrow energy range, the library of minima sampled in the reminimisation step is expanded to all which lie within 200 meV of the putative GM. This relaxation of the usual, generation-based criteria was found to be necessary to capture sufficient structural diversity. For neutral clusters, a slightly different approach was employed. The BCGA results generated in the study of Heiles et al. [29] are used as a first approximation to the putative database of cluster structures. This database was then expanded to include homotops of every structural class represented by the clusters of Heiles et al., in order to diversify the structural space considered, and capture any missing permutational isomers. Planarity/non-planarity of resulting local minima is determined by individual inspection of local minima after the final geometry optimisation. It is important to note that small distortions due to such features as vibronic coupling are not captured with our calculation method.

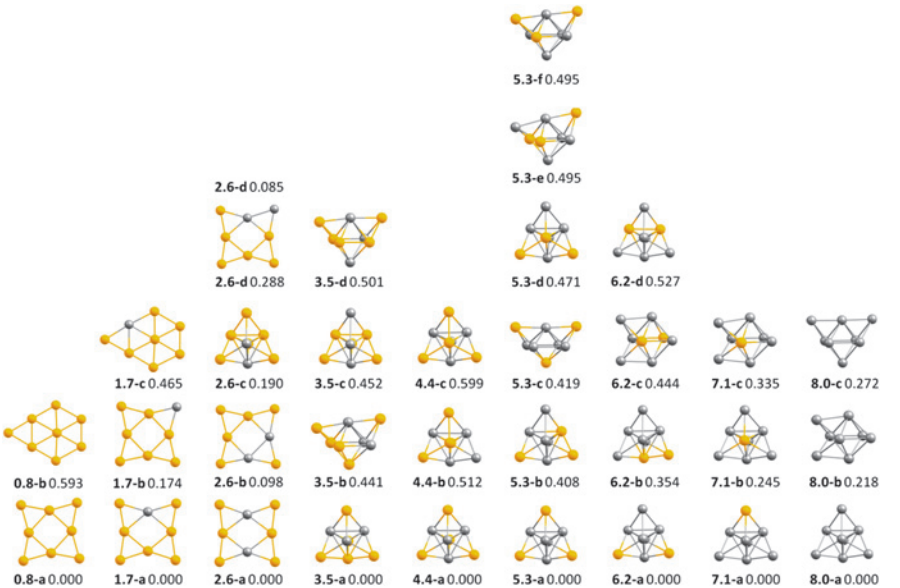

Figure 1: GM isomers of neutral Ag_nAu_m $(n + m = 8)$ clusters and first suboptimal isomers.The number of Ag and Au atoms in each cluster Ag_nAu_m are given in bold. The relative energies are given in eV.

3 Results and discussion

3.1 Neutrals

The global minima and energetically low-lying suboptimal minima for the neutral Ag_nAu_m case are depicted in Figure 1. At the endpoint of the compositions, the gold octamer adopts the planar, tetra-bridged square motif (alternatively described as a leaf structure), with D_{4h} symmetry [29, 45–47]. The presence of planar gold clusters to $m = 7$ is well observed both theoretically and experimentally, while the competition between D_{4h} and compact, nugget-like motifs has been investigated in the literature for the $m = 8$ cluster. The role of relativistic effects is known to be significant in gold-based cluster systems, and manifests itself structurally, by driving a 2D–3D transition which occurs at larger sizes than in other metals. This effect can be attributed to the balance between enhanced aurophilicity, which acts to bind in a compact, highly coordinated manner, and the increased valence orbital hybridisation, which acts to enhance planarity. The capture of dispersive effects with M06-L is noted by Serapian et al. [47] to overestimate the

Au–Au bonding and induce 3D structures, while PBE and CCSD(T) calculations give the 2D structure. The conclusion that the 2D geometry is the true GM is drawn. Furthermore, methods which sufficiently reproduce the s-d hybridisation, but do not overestimate dispersion should achieve this result. We observe that the neutral Au_8 cluster indeed retains the 2D structure, implying that the aurophilicity is not overestimated with the current method, and it may be appropriate for these small, gold-based clusters. The present findings, calculated with a range separated PBEh functional, show a distinct preference for the planar motif, with no 3D structures within 0.6 eV of the GM. In the above reference, and those cited therein, explicit spin-orbit corrections are commonly neglected, as in the current work, which may lead to some numerical error, although scalar relativistic effects are included.

For Ag_8, the tetra-capped tetrahedral (TcTd) motif is preferred, as reported by several authors [29, 30, 48]. While the delicate balance between 2D and 3D motifs in gold is driven by the significant, relativistic valence s/d orbital hybridisation, silver exhibits a large 6s–5d gap in the valence band, and thus is more accurately described as an s-metal. The pseudo-spherical symmetry of the TcTd motif thus maximises s orbital overlap in bonding, whilst filling the complete Jellium 1P shell, and means that 2D isomers are non-competitive for the neutral Ag_8 cluster.

The structural trend across compositions is simple for the neutral cluster, with TcTd motifs dominant for all compositions which contain fewer than six gold atoms, beyond which, the preference switches to the planar leaf structure. This transition is observed to be well-defined and abrupt, with planar motifs not observed in the low-energy region for silver-rich motifs, and a 3D structure only found in the gold-rich regime once, at +0.19 eV for Ag_2Au_6. As a result, at Ag_2Au_6, the 2D–3D gap is 0.19 eV, and at Ag_3Au_5, is > 0.50 eV. It should be expected on the basis of these calculations that there should be little coexistence of isomers with differing dimensionalities in an experiment with well-defined cluster composition. The preferred structural isomer for the neutral clusters, is thus related to the structure of the monometallic global minima, as found in previous DFT studies on similar Au–Ag clusters [21, 49].

For intermediate compositions, it is valuable to consider not just the position of the 2D–3D transition, as a measure of the relative importance of both dopant metals, but the permutational isomeric preferences displayed across the range. While the structural preference for each cluster is straightforward, the occupation of atomic sites upon a given cluster is a complex effect. In a previous article we discussed the balance of first and second order charge transfer effects [17]. Geometric frustration leads to inherent charging upon sites, which are occupied by atoms that satisfy the preferred charge state. Additionally, the effect of one atom upon

its neighbours gives rise to the second order effect, for which relative electronegativity plays a significant role. This description of charging effects was used to explain the complex preference of gold and silver dopants on the tetrameric clusters $Ag_nAu_{(4-n)}^+$, in which gold preferentially occupied low-coordinate sites, except in the highly frustrated y-shape motifs, in which the high-coordination central site was take up by gold, to maximise charge transfer from silver atoms. For the neutral Ag_nAu_m clusters considered here, there is negligible difference in the atomic radii, so we expect charge effects to dominate homotop preference. With a Pauling electronegativity of 2.5 (c.f 1.9 for Ag), Au atoms occupy sites which attain maximal negative charge, which in the case of the TcTd motif, is the external, capping atom sites, as evidenced by a previous study on neutral CuAg octamers. As a result, the trend on increasing gold doping into the silver cluster, is one in which the gold atoms decorate the outer shell, leaving the high coordination sites to a silver "core". When the gold doping is sufficient to cause the 2D–3D transition, silver atoms occupy maximally coordinated, central sites, which maximises charge transfer. This was observed in an early DFT study of bimetallic gold-silver clusters by Bonačić-Koutecký et al. [21], who also find the same homotop preference. Despite seeding our reminimisation step with a large number of additional homotops, we do not find any clusters which improve on those results. This agreement implies that the BCGA represents a good method for the location of such small bimetallic clusters, while additionally suggesting that variation of the xc-functional to include range-dependent Hartree–Fock exchange does not drastically alter the energy landscape. It is of note, however, to consider that at the 2D–3D transition, the LC-ωPBEh energies show a larger separation. Heiles et al. report a difference of 39 meV between isomer **2.6a** and **2.6c**, whereas the present result is 190 meV.

The binding energy E_b is defined as:

$$E_b = -\frac{E(Ag_nAu_m) - nE(Ag_1) - mE(Au_1)}{n+m} \tag{1}$$

such that an increase in the positive direction represents an enhanced degree of cohesion. The binding energies of the monometallic species may be compared with their bulk values of 3.81 eV and 2.5 eV for Au and Ag, respectively. Assadollahzadeh and Schwerdtfeger found E_b = 1.79 eV for Au_8 with a DFT genetic algorithm study [46], in close agreement with our reported value of 1.74 eV. Other authors have reported binding energies between 3 and 13% higher for the same structure with various basis sets and with both GGA [47, 50] and meta-GGA [47] functionals. For the Ag_8 cluster, the present value of 1.41 eV is again lower than the corresponding PBE value (for the identical structure), of 1.58 eV [29].

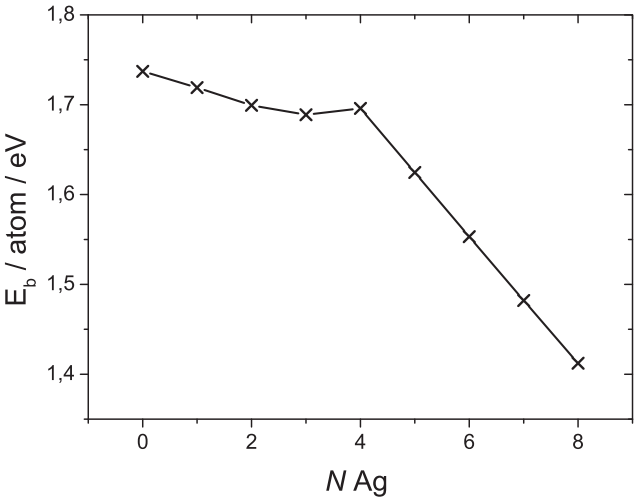

Figure 2: Binding energies for the GM isomers of the neutral clusters.

The trend across the composition range, as depicted in Figure 2, shows a simple variation which follows the structural preference of the GMs. From Au_8 to Ag_2Au_6, there is a linear decrease in binding energy, as the silver atoms contribute less to the total cohesion, and are arranged in the structure of the Au_8 cluster GM. From Ag_4Au_4 to Ag_8, the trend is again a linear decrease, as gold atoms are replaced in a direct substitution manner, into the Ag_8 GM structure. We may therefore quantify the energetic cost to cohesion of individual elemental substitutions. Replacement of gold with silver in the D_{4h} leaf structure costs 19 meV per dopant, and replacement of gold with silver in the TcTd structure costs 71 meV per dopant. The exception to these trends is the intermediate composition Ag_3Au_5, for which the TcTd structure is maintained, but is not more stable than Ag_4Au_4. In part, this is because the high symmetry 1 : 1 TcTd structure is particularly stable, maximising charge transfer and minimising strain. Additionally, replacing a silver atom with a gold to form Ag_3Au_5 induces significant strain, as the electronic driving force towards planarity in gold becomes important.

3.2 Cations

The GM structures of the mono-cationic species $Ag_mAu_m^+$ display both a closer competition between isomers and a richer library of structures than the neutral case. The structural symmetry of the cluster is reduced from the pseudo-spherical

TcTd motif which dominates for the neutral cluster, producing a greater variety of possibilities due to the open spin and Jellium shells. For the pure silver cluster, the TcTd is not found within the lowest energy structures, and is replaced by the mono-capped pentagonal biprism (McPB), the defect tetrahedron (d-TcTd) and the bicapped octahedron (BcOh), each of which are commonly found motifs for clusters of this size. The close energetic competition between structures means it cannot be definitely stated which is the global minimum, and the range of clusters depicted in Figure 3 should be considered an ensemble of essentially isoenergetic structures, each of which is likely to be available in an experiment at non-negligible temperature. However, trends may qualitatively be made regarding the 2D–3D transition and permutational isomer preference. It is clear that, in alignment with the neutral clusters, gold atoms decorate the external, low coordination sites on the silver framework. This may be noted from examination of the $Ag_7Au_1^+$ cluster. Of the three geometries found within 0.1 eV of the GM, the BcOh, McPB and d-TcTd, the single gold atom is found to occupy three and fourfold sites, despite the availability of five and sixfold sites. For the BcOh cluster, the first instance of gold occupying the central fivefold site is at cluster **3.5-d**, ($Ag_3Au_5^+$), for which there is no alternative arrangement. For McPB, the corresponding cluster is **4.4-b** ($Ag_4Au_4^+$), where a gold atom takes a sixfold site. The gold-rich range is controlled by the open, winged structure which is found to be the GM for all compositions with more than 4 gold atoms. As in the neutral case, the silver atoms preferentially occupy the central, high-coordination sites. For the pure gold cluster, the close competition between planar and compact motifs is in line with previous works which debate the position of the 2D–3D transition in cationic gold. While for the neutral cluster the transition is certainly above the octamer in size, it is less clear for the cation, which is known to have an increased propensity towards compact structures. The present results suggest that $m = 8$ is the balancing point between 2D and 3D isomers. This energetic similarity is the reason why planar motifs are not observed in the low-energy region of configuration space for any compositions which contain silver. A single dopant is sufficient to drive the transition entirely towards 3D geometries.

3.3 Anions

For anionic clusters, the Jellium 1D orbital becomes singly occupied. We might therefore expect a greater preponderance of elongated, prolate structures, which include asymmetric planar motifs, in line with the description of de Heer [51] and thus a change in the position of the 2D–3D transition to higher silver loading. Figure 4 displays the most stable structures found with our two-phase GA + LC-

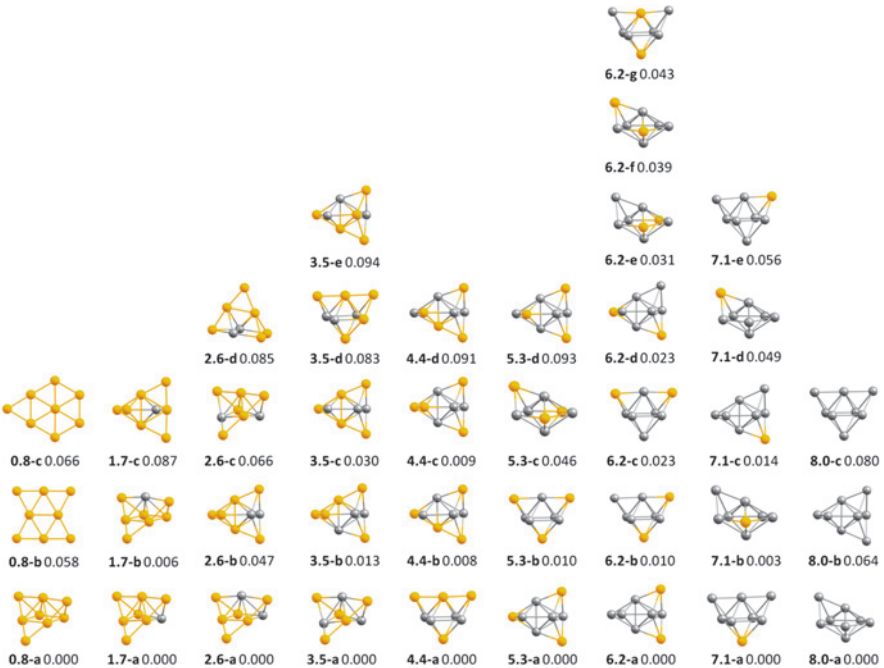

Figure 3: Isomers of cationic $Ag_nAu_m^+$ $(n + m = 8)$ clusters within 0.1 eV. There is a close competition between isomers within this small threshold.

ωPBEh method. It is observed that indeed, the 2D–3D transition is moved dramatically to the silver-rich regime, with the first three dimensional GM at $Ag_6Au_2^-$. For the two mixed compositions which do not adopt planar structures, the bridged pentagonal bipyramidal structure is preferred, which may be thought of as a pseudoplanar geometry. It is interesting to note that this drive to take pseudoplanar motifs, and for gold atoms to take low coordination sites is so strong that, for these pentagonal bipyramidal clusters, the gold atom bridges two silver atoms, rather than occupying the threefold capping site, which is 0.16 eV higher in energy for $Ag_6Au_2^-$ and 44 meV higher for $Ag_7Au_1^-$. For the planar motifs, the leaf structure is, in common with the neutral species, the preferred isomer. The occupation of sites by silver is again noted to be controlled by the need to avoid low coordination sites. All homotops for which silver atoms are constrained to the four central sites are located, and each is within 50 meV of the GM. In fact, only for the 1 : 1 composition is a homotop which places a silver outside the central four sites found (**4.4b**). This homotop is destabilised relative to the GM by 0.28 eV. The drive towards planarity is the key feature in predicting anionic mixed cluster structure.

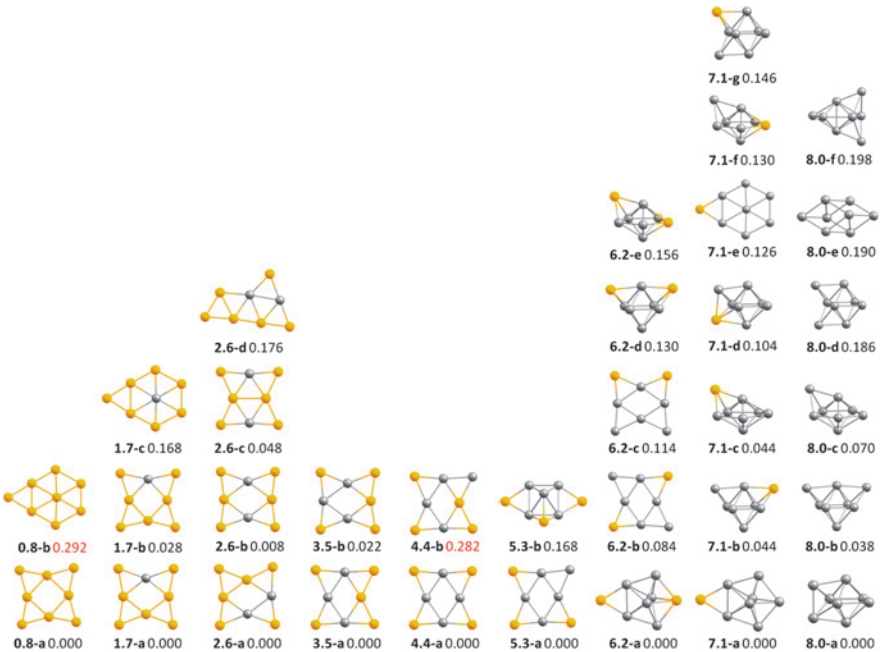

Figure 4: Isomers of anionic $Ag_nAu_m^-$ $(n + m = 8)$ clusters within 0.2 eV. Compositions for which there is only one isomer within 0.2 eV have an additional structure included, with its relative energy depicted in red.

3.4 Energetics

Energetic analysis of the stability of a dopant series with respect to disproportionation is useful in order to locate the thermodynamically preferred composition. For this purpose, the mixing energy E_m is used, and is defined in Equation (2) for a bimetallic cluster of n A atoms, and m B atoms, as:

$$E_m(Ag_nAu_m) = E(Ag_nAu_m) - \frac{nE(Ag_{n+m}) - mE(Au_{n+m})}{n+m} \quad (2)$$

where $E(X_{n+m})$ is the energy of the monometallic GM cluster of element X, at the same size.

All compositions which are stable with respect to disproportionation into their monometallic GM counterparts have a negative value of E_{mix}. Figure 5 shows the mixing energy profiles for each of the three charge states considered. For the neutral cluster, every composition is stable with respect to the pure clusters: in agreement with the propensity towards mixing found in the bulk, where there

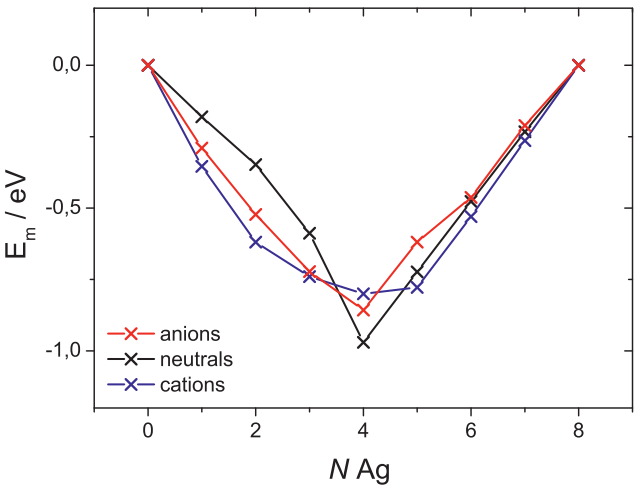

Figure 5: Mixing energies for the GM clusters across all compositions and charge states.

is no miscibility gap for gold-silver alloys. For the silver-rich regime, the trend is a linear, monotonic increase in stability as doping increases, while the maximally mixed cluster, Ag_4Au_4 is the preferred composition; in line with the result of Heiles et al. [29]. The next cluster in the series, Ag_3Au_5, is however, significantly destabilised, implying an energetic competition between the 3D structural preference of Ag and the 2D preference of Au. While there are sufficient silver atoms to promote the TcTd motif, the strain induced by the gold atoms reduces the overall stability of this structure. This effect is apparent in the binding energy curve, which exhibits the same discontinuity beyond the 1 : 1 composition. The resulting asymmetry in the E_{mix} curve is therefore a reflection of the asymmetry in the 2D–3D transition, for which silver has the strongest influence. Comparing the mixing energy to previous PBE results shows excellent agreement, both in overall preference and the shape of the profile. This suggests that the range-separated functional gives a consistent description across the entire doping series, and differs only by enhancing the mixing energies slightly. For example, Ag_4Au_4 has an E_{mix} of −0.97 eV, as compared to −0.81 eV in Reference [29].

For the cationic clusters the trend is qualitatively similar, with each composition stable with respect to disproportionation, and the 1 : 1 composition optimal overall. However, there is significantly closer competition between compositions, with the E_{mix} varying by only 60 meV between Ag_3Au_5 and Ag_5Au_3. The absolute values of the mixing energy suggest that for silver-rich clusters, the inclusion of gold atoms, spaced such that they occupy low coordination sites and avoid Au–Au bonds, provides an approximately constant stability gain of around

0.2 eV, regardless of the details of the cluster structure. In the gold-rich region, the cationic E_{mix} are greater in magnitude than for the neutral cluster, which is due to the suppression of the competition observed in the neutral case. As the 3D isomer is globally stable across all compositions, there is less of an energetic penalty for decorating gold atoms on a compact geometry, and so mixing energies are significantly greater.

The anionic cluster exhibits the simplest mixing energy curve, with a largely symmetric profile centred on the 1 : 1 composition, which as for the cationic and neutral clusters, is the most stable composition with respect to the monometallic endpoints. From the gold cluster, the sequential addition of silver atoms imparts a relatively invariant stabilisation of 0.25–0.3 eV per silver atom. This stabilisation is due to the inclusion of charge donors in high coordination sites, which maximises the charge transfer to gold atoms in the bridging locations. For the 1 : 1 composition, this effect becomes saturated, such that an additional gold atom would reduce the charge transfer, and be forced into an unfavourable central site, and an additional silver atom would be forced into an unfavourable bridging site. Starting from the silver cluster end of the composition range, it should be noted that the trend follows that of the cationic and neutral clusters closely. E_{mix} increases in magnitude for every gold dopant, towards $Ag_4Au_4^-$, largely independently of the structure. A kink occurs for $Ag_5Au_3^-$, at which the first planar GM is found. This point along the composition range exhibits the strain between 2D and 3D structures previously noted for the Ag_3Au_5 neutral cluster.

It is clear overall that despite the difference in structural variation between the gold-rich and the silver-rich composition regimes, there is close agreement in the mixing energies. E_{mix} is affected much less by the structure of the cluster than the level of doping. Only at compositions on the cusp of the 2D–3D transition are there notable differences from the "v-shape" curve, while the optimal composition is invariant to charge state for the considered clusters. One should expect fully mixed clusters regardless of the cluster charge, as each charge state allows for a mixing energy of between 0.8 and 1.0 eV.

The global optimisation approach within DFT neglects an explicit treatment of entropy. It has been shown for larger coinage metal clusters that entropy may play some role in controlling the relative depths of free energy wells, and thus the favourability of particular minima [52, 53]. As a result, calculations which neglect these effects should be considered to be representative of a low temperature regime, such as that of a sparse cluster beam experiment.

3.5 Vertical ionisation potentials and detachment energies

The vertical ionisation potential is defined simply as

$$\mathrm{vIP}(\mathbf{R}) = E(\mathrm{Ag}_n\mathrm{Au}_m(\mathbf{R}))^{\nu+1} - E(\mathrm{Ag}_n\mathrm{Au}_m(\mathbf{R}))^{\nu} \tag{3}$$

where $\mathbf{R}$ is a coordinate vector which defines the atomic positions and ν is an arbitrary charge state, either 0 in describing the vertical ionisation potential (vIP), or −1 in describing the vertical detachment energy (vDE), while $\mathbf{R}$ is kept fixed in all cases.

Accurate prediction of detachment energies allows for the structurally precise assignment of clusters in experiment, through comparison with photoelectron spectroscopy for $\nu = -1$.

In Figure 6, the vIPs for the entire composition range of the neutral cluster are displayed, for both the global minima and the first suboptimal minima. For the GM structures, the vIP increases in a manner similar to the binding energies. Each additional gold atom inserted into TcTd structure in replacement of a silver atom, increases the IP, up to a maximum value of 7.72 eV for the most stable neutral cluster, $\mathrm{Ag}_4\mathrm{Au}_4$. A reduction in vIP follows the addition of the fifth gold atom, which destabilises the cluster. For the gold-rich, planar isomers, the vIP is largely independent of silver doping, and reaches a maximum at Au_8, of 8.07 eV, which is in excellent agreement with CCSD(T) calculations (between 7.96 and 8.10 eV) [54], and with the result of Assadollahzadeh et al. of 8.01 and 8.14 eV, calculated with two different basis sets [46]. For the Ag_8 endpoint, the calculated vIP is 6.70 eV, which is comparable with the recently calculated PBE value of 6.4 eV reported by Gamboa et al. [55].

The second vIP curve (depicted in red on Figure 6) corresponds to the values as calculated from the first suboptimal minima. For the neutral cluster, there is a clear and significant separation between the GM and the higher energy isomers for all compositions except $\mathrm{Ag}_2\mathrm{Au}_6$. The sensitivity is greater for the planar clusters than those which adopt the TcTd motif, as evidenced by $\mathrm{Ag}_2\mathrm{Au}_6$ and $\mathrm{Ag}_1\mathrm{Au}_7$. For these clusters, relocation of the silver dopant leads to a change of 0.20 eV and 0.24 eV, respectively. The most striking variation is between the two planar Au_8 isomers. From the D_{4h} leaf to the bridged hexagon induces a decrease of 0.5 eV, which further supports the prediction of the leaf structure as the GM.

Figure 7 depicts the vertical detachment energy for the anionic clusters as a function of composition. This curve shows sharp variations on doping, with a dramatic increase in vDE once the first gold atom is incorporated into the cluster. There is another step in the curve at $\mathrm{Ag}_3\mathrm{Au}_5^-$, at which point the vDE essentially becomes saturated at the value for the gold anion (2.35 eV). This Au_8^- vDE may be compared with the experimental value of 2.79 eV, and the theoretical results of

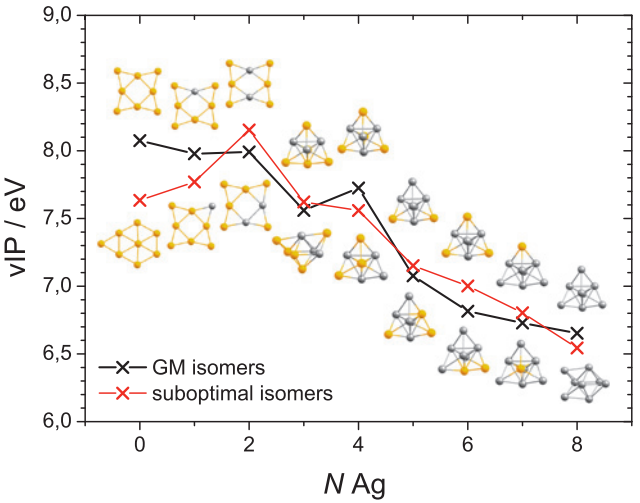

Figure 6: Vertical ionization potentials for the optimal and first suboptimal isomers of the neutral clusters.

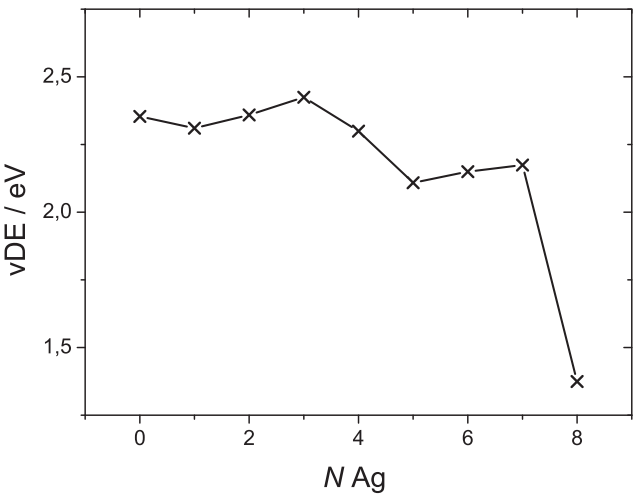

Figure 7: Vertical detachment energies for the GM isomers of the anionic clusters.

Hakkinen and Landman (2.56) eV [56], although the latter authors reported a 3D structure for the Au_8^- cluster. The same authors later calculated vDEs for several sizes of anionic gold cluster with large kinetic energy cutoffs and the PBE xc functional, and included the leaf structure, resulting in a slight overestimation

(2.92 eV) [57]. Clearly the LCωPBEh functional causes a reduction in the vDE with respect to the pure GGA functional.

Ho et al. report an Ag_8^- vertical detachment energy of 1.65 ± 0.05 eV with photoelectron spectroscopy [58], while Ganteför et al. obtain a value of 1.5 ± 0.1 eV for the same cluster [59]. Our calculations are in reasonable agreement, with a value of 1.37 eV. The underestimation is therefore apparent, but less significant for silver than gold clusters.

For intermediate compositions, where the stepwise increase in vDE occurs, the curve can be explained by comparison to the mixing energy profile. Doping of gold into silver induces an increase in vDE, analogous to the increase in vIP observed for the neutral cluster. This increase is largely independent of gold concentration until the structural change occurs at $Ag_5Au_3^-$. Clearly, beyond this composition, the vDE is essentially unaffected by silver loading, and is an artefact of the unchanging chemical environment around the gold atom from which the electron is removed.

It is well known that the vDEs may be very sensitive to the structure of a cluster, and this sensitivity is in fact observed for the $Ag_7Au_1^-$ cluster, for which the first suboptimal minimum **7.1b** is a bicapped octahedral motif, and exhibits a vDE of 1.56 eV, which is 0.61 eV lower than the value for the GM. Clearly the absolute values of ionization potential and detachment energies are a more subtle and precise measure of the isomer present in an experiment than the predictions made by mixing energy. While the latter allows for the prediction of composition, and is largely invariant to precise structure, the vDE value is likely to finely measure which isomer is observed. It would be of great interest to obtain experimental vDE and vIP data on these ultrasmall mixed clusters from experiment in order to test such a prediction. It would be reasonable to expect significant variation in vDE between different homotops for a given structure, in the case of multimetallic species. However, as is observed for the entire range of cationic bimetallic clusters, this effect is in fact relatively small. Therefore, in general we can conclude that the structure without the precise homotop should be sufficient to make reasonable predictions of ionisation potentials.

3.6 2D–3D transition

The position of the 2D–3D transition along the dopant series is sensitively dependent on charge state. For the neutral system, the transition is found to be well-defined, and exhibits a notably larger 2D–3D separation in the compositions around the transition than PBE calculations on the same system. This effect, which is directly due to the range separation of exchange in the current functional,

serves to narrow down the possible isomers available at low energies. The direct effect of the range separation in configurational preference is also noted in the separation between 2D and 3D isomers for neutral Au_8. Serapian et al. [47] provided a comprehensive analysis of the balance between GGA and meta-GGA functionals in their structure prediction. M06-L, a local meta-GGA functional with 0% Hartree–Fock exchange represents an effort to include long range effects, known to have a drastic impact on the stability of metallic structures. In the present work, we utilise a method which may be considered a combination of the two: a hybrid GGA functional, with a long range Hartree–Fock exchange term to capture long-range effects in the xc term. It is interesting therefore to note that our results for Au_8 agree more closely with PBE than M06-L. This may be due to the limited extent of long range interactions in such small clusters, although it has been previously shown that such a functional can have a marked effect in even smaller, tetrameric Au, Ag, and Au–Ag clusters [16, 17].

While the effect on structural preference is modest, a justification of the use of range corrected functionals is found in charged species, either in the optimisation of cationic and anion clusters, or in the calculation of vIPs, which have been widely discussed as an area in which such functionals are valuable. Good agreement with higher level electronic structure calculations has been found, where available, for the neutral clusters, suggesting a less computationally demanding procedure for the accurate analysis of spectroscopic experiments.

For the charged species, it is observed that there is no clear global minimum structure, nor preferred composition, so discussion of the structures must be made in a broad, ensemble sense. The overall trend of planar gold-rich motifs, converting into compact silver-rich structures remains throughout the charge series, while the choice of permutational isomers is dominated by the electronic stabilisation afforded by maximising charge transfer from silver to gold. In most cases, this corresponds to the location of gold atoms on low coordination sites on the exterior of the cluster, which maximises heterobonding whilst simultaneously minimising Au–Au bonding.

It is of particular note however, that in spite of a lack of a clear GM, the overall energetic trends, in which mixing energy is maximised at the 1 : 1 composition, is unaffected. Figure 8 shows the existence of a hierarchy of effects. Starting from the neutral Ag_4Au_4 cluster, we may replace silver with gold, gold with silver, or add or subtract charge from the cluster. It should be noted that the charge has much more influence on the final structure than does the extent of doping. A change of charge state is sufficient to unambiguously drive 2- or 3-dimensionality. It is interesting that for the 1 : 1 compositions at each charge state, the principle of maximum symmetry applies to the given structure, with the formation of a complete Ag_4 core, surrounded by an Au_4 shell, apparent in each case. For the neutral cluster, this

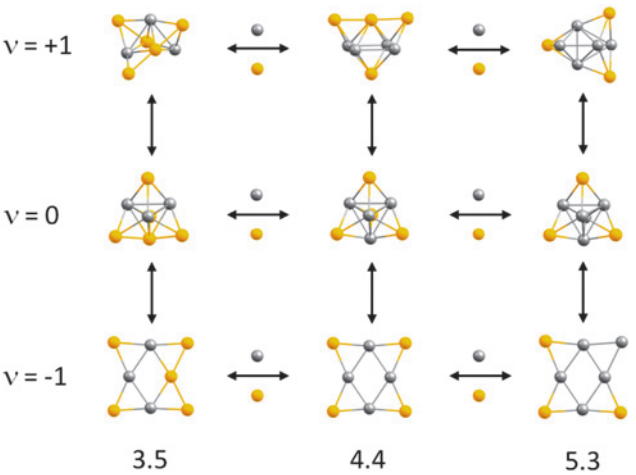

Figure 8: The GM isomers of a selection of clusters, showing the effect of charge state and doping on the maximally mixed cluster.

takes the form of a core-shell tetracapped tetrahedron. For the anion, the concept of core and shell is reduced to a 2D manifold, with silver atoms surrounded by bridging gold. For the cation, the Ag_4 unit is again clear, suggesting that this is a general feature of the highly mixed AuAg clusters, regardless of charge state, and is a contributing factor towards the special stability of the 1 : 1 composition.

4 Conclusions

A DFT global optimisation study has been undertaken to determine the structures, permutational isomers and energetic properties of a unique ultrasmall cluster system. Gold-silver octamers represent a finely balanced cluster size, with a 2D–3D structural transition which is sensitively dependent on charge state and dopant loading. It is observed that varying charge from +1 to −1 moves the position of this transition across the full range. Comparison of ionisation potentials and mixing energies agree well with available experimental and high level electronic structure results, predicting 1 : 1 mixed clusters for all charge states. Competition between structural isomers is found to vary between charge states, with well-defined global minima for neutral clusters, and a complex coexistence of several isomers for the charged species, indicating a charge-dependent roughing of the energy landscape. While structure is more dependent on charge than dopant loading,

the overall stability, as measured by mixing energy, is largely invariant to both charge and structure, changing only with doping level.

Acknowledgement: The calculations reported here have been performed on the following HPC facilities: The University of Birmingham BlueBEAR facility (Reference [61]); the MidPlus Regional Centre of Excellence for Computational Science, Engineering and Mathematics, funded under EPSRC grant EP/K000128/1 (R.L.J.); and via our membership of the UK's HPC Materials Chemistry Consortium, which is funded by EPSRC (EP/L000202), this work made use of the facilities of HECToR and ARCHER, the UK's national high-performance computing service, which is funded by the Office of Science and Technology through EPSRC's High End Computing Programme.

A. S. and R. S. acknowledge financial support by the DFG (grant SCHA 885/10-2) and the Merck'sche Gesellschaft für Kunst und Wissenschaft e.V. The authors are thankful for the input of Sven Heiles, who provided optimised neutral cluster structures, and for useful discussions throughout this work.

References

1. J. K. Gansel, M. Thiel, M. S. Rill, M. Decker, K. Bade, V. Saile, G. von Freymann, S. Linden, and M. Wegener, Science **325** (2009) 1513.
2. S. Wang, X. Meng, A. Das, T. Li, Y. Song, T. Cao, X. Zhu, M. Zhu, and R. Jin, Angew. Chem. Int. Edit. **53** (2014) 2376.
3. M. Käll, Nat. Mater. **11** (2012) 570.
4. M. V. Petri, R. A. Ando, and P. H. Camargo, Chem. Phys. Lett. **531** (2012) 188.
5. T. J. A. Slater, A. Macedo, S. L. M. Schroeder, M. G. Burke, P. O'Brien, P. H. C. Camargo, and S. J. Haigh, Nano Lett. **14** (2014) 1921.
6. N. L. Rosi and C. A. Mirkin, Chem. Rev. **105** (2005) 1547.
7. M. Larguinho and P. V. Baptista, J. Proteomics **75** (2012) 2811.
8. D. R. Kauffman, D. Alfonso, C. Matranga, H. Qian, and R. Jin, J. Phys. Chem. C **117** (2013) 7914.
9. C. Kumara, C. Aikens, and A. Dass, J. Phys. Chem. Lett. **5** (2014) 461.
10. J. C. Fabbi, J. D. Langenberg, Q. D. Costello, M. D. Morse, and L. Karlsson, J. Chem. Phys. **115** (2001) 7543.
11. Y. Negishi, Y. Nakamura, A. Nakajima, and K. Kaya, J. Chem. Phys. **115** (2001) 3657.
12. W. Huang and L.-S. Wang, Phys. Chem. Chem. Phys. **11** (2009) 2663.
13. W. Huang and L.-S. Wang, Phys. Rev. Lett. **102** (2009) 153401.
14. L.-M. Wang, R. Pal, W. Huang, X. C. Zeng, and L.-S. Wang, J. Chem. Phys. **132** (2010) 114306.
15. S. Gilb, K. Jacobsen, D. Schooss, F. Furche, R. Ahlrichs, and M. M. Kappes, J. Chem. Phys. **121** (2004) 4619.
16. A. Shayeghi, R. L. Johnston, and R. Schäfer, Phys. Chem. Chem. Phys. **15** (2013) 19715.

17. A. Shayeghi, C. J. Heard, R. L. Johnston, and R. Schäfer, J. Chem. Phys. **140** (2014) 054312.
18. M. Haertelt, V. J. F. Lapoutre, J. M. Bakker, B. Redlich, D. J. Harding, A. Fielicke, and G. Meijer, J. Phys. Chem. Lett. **2** (2011) 1720.
19. C. Kerpal, D. J. Harding, A. C. Hermes, G. Meijer, S. R. Mackenzie, and A. Fielicke, J. Phys. Chem. A **117** (2013) 1233.
20. P. Weis, O. Welz, E. Vollmer, and M. M. Kappes, J. Chem. Phys. **120** (2004) 677.
21. V. Bonačić-Koutecký, J. Burda, R. Mitrić, M. Ge, G. Zampella, and P. Fantucci, J. Chem. Phys. **117** (2002) 3120.
22. P. Koskinen, H. Häkkinen, B. Huber, B. von Issendorf, and M. Moseler, Phys. Rev. Lett. **98** (2007) 015701.
23. M. Neumaier, F. Weigend, O. Hampe, and M. M. Kappes, J. Chem. Phys. **125** (2006) 104308.
24. I. Fleischer, D. M. Popolan, M. Krstić, V. Bonačić-Koutecký, and T. M. Bernhardt, Chem. Phys. Lett. **565** (2013) 74.
25. G.-F. Zhao, J.-M. Sun, and Z. Zeng, Chem. Phys. **342** (2007) 267.
26. X.-D. Zhang, M.-L. Guo, D. Wu, P.-X. Liu, Y.-M. Sun, L.-A. Zhang, Y. She, Q.-F. Liu, and F.-Y. Fan, Int. J. Mol. Sci. **12** (2011) 2972.
27. X. López-Lozano, C. Mottet, and H.-C. Weissker, J. Phys. Chem. C **117** (2013) 3062.
28. H.-Ch. Weissker, R. L. Whetten, and X. López-Lozano, Phys. Chem. Chem. Phys. **16** (2014) 12495.
29. S. Heiles, A. J. Logsdail, R. Schäfer, and R. L. Johnston, Nanoscale **4** (2012) 1109.
30. C. J. Heard and R. L. Johnston, Eur. Phys. J. D **67** (2013) 34.
31. F. Munoz, A. Varas, J. Rogan, J. A. Valdivia, and M. Kiwi, Phys. Chem. Chem. Phys. **17** (2015) 30492.
32. S. Heiles and R. L. Johnston, Int. J. Quantum. Chem. **113** (2013) 2091.
33. P. Giannozzi, S. Baroni, N. Bonini, M. Calandra, R. Car, C. Cavazzoni, D. Ceresoli, G. L. Chiarotti, M. Cococcioni, I. Dabo, A. Dal Corso, S. de Gironcoli, S. Fabris, G. Fratesi, R. Gebauer, U. Gerstmann, C. Gougoussis, A. Kokalj, M. Lazzeri, L. Martin-Samos, N. Marzari, F. Mauri, R. Mazzarello, S. Paolini, A. Pasquarello, L. Paulatto, C. Sbraccia, S. Scandolo, G. Sclauzero, A. P. Seitsonen, A. Smogunov, P. Umari, and R. M. Wentzcovitch, J. Phys. Condens.-Mat. **21** (2009) 395502.
34. R. L. Johnston, Dalton T. (22) (2003) 4193.
35. A. M. Rappe, K. M. Rabe, E. Kaxiras, and J. D. Joannopoulos, Phys. Rev. B **41** (1990) 1227.
36. J. Perdew, K. Burke, and M. Ernzerhof, Phys. Rev. Lett. **77** (1996) 3865.
37. M. Methfessel and A. T. Paxton, Phys. Rev. B **40** (1989) 3616.
38. M. Valiev, E. J. Bylaska, N. Govind, K. Kowalski, T. P. Straatsma, H. J. J. Van Dam, D. Wang, J. Nieplocha, E. Apra, T. L. Windus, and W. A. de Jong, Comput. Phys. Commun. **181** (2010) 1477.
39. F. Weigend and R. Ahlrichs, Phys. Chem. Chem. Phys. **7** (2005) 3297.
40. M. A. Rohrdanz, K. M. Martins, and J. M. Herbert, J. Chem. Phys. **130** (2009) 054112.
41. D. W. Silverstein and L. Jensen, J. Chem. Phys. **132** (2010) 194302.
42. J. V. Koppen, M. Hapka, M. M. Szczśniak, and G. Chaasiski, J. Chem. Phys. **137** (2012) 114302.
43. F. Rabilloud, J. Phys. Chem. A **117** (2013) 4267.
44. O. A. Vydrov and G. E. Scuseria, J. Chem. Phys. **125** (2006) 234109.
45. E. Fernández, J. Soler, I. Garzón, and L. Balbás, Phys. Rev. B **70** (2004) 165403.
46. B. Assadollahzadeh and P. Schwerdtfeger, J. Chem. Phys. **131** (2009) 064306.
47. S. A. Serapian, M. J. Bearpark, and F. Bresme, Nanoscale **5** (2013) 6445.

48. V. Bonačić-Koutecký, V. Veyret, and R. Mitrić, J. Chem. Phys. **115** (2001) 10450.
49. R. Mitrić, C. Bürgel, J. Burda, V. Bonačić Koutecký, and P. Fantucci, Eur. Phys. J. D. **24** (2003) 41.
50. A. V. Walker, J. Chem. Phys. **122** (2005) 094310.
51. W. A. de Heer, Rev. Mod. Phys. **65** (1993) 611.
52. A. Vargas, G. Santarossa, M. Iannuzzi, and A. Baiker, Phys. Rev. B **80** (2009) 195421.
53. E. C. Beret, L. M. Ghiringhelli, and M. Scheffler, Faraday Discuss. **152** (2011) 153.
54. R. M. Olson and M. S. Gordon, J. Chem. Phys. **126** (2007) 214310.
55. G. U. Gamboa, A. C. Reber, and S. N. Khanna, New. J. Chem. **37** (2013) 3928.
56. H. Häkkinen and U. Landman, Phys. Rev. B **62** (2000) R2287.
57. H. Häkkinen, S. Abbet, A. Sanchez, U. Heiz, and U. Landman, Angew. Chem. **115** (2003) 1335.
58. J. Ho, K. M. Ervin, and W. C. Lineberger, J. Chem. Phys. **93** (1990) 6987.
59. G. Ganteför, M. Gausa, K.-H. Meiwes-Broer, and H. O. Lutz, J. Chem. Soc. Faraday T. **86** (1990) 2483.
60. A. Shayeghi, D. Götz, J. B. A. Davis, R. Schäfer, and R. L. Johnston, Phys. Chem. Chem. Phys. **17** (2015) 2104.
61. See http://www.bear.bham.ac.uk/bluebear.